# Flow modes provide a quantification of *Physarum* network peristalsis

Ryan Wilkinson [a,*], Matthew Koziol [a], Karen Alim [b], Marcus Roper [a,c]

[a] *UCLA Dept. of Mathematics, USA*
[b] *Technische Universität München Dept. of Physics, Germany*
[c] *UCLA Dept. of Computational Medicine, USA*

## ARTICLE INFO

## ABSTRACT

*Physarum polycephalum* is a foraging, network-forming organism known for its ability to make complex decisions and maintain memory of past stimuli without use of a complex nervous system. Self-organized peristaltic flows within the network transport nutrients throughout the organism and initiate locomotion and morphological changes. A key step in understanding *P. polycephalum*'s ability to change behavior is therefore forming descriptors of this peristaltic flow. Here, we develop a dynamic network-based method for describing organism-wide patterns of tube contractions from videos of *P. polycephalum*. Our tool provides robust readouts of the diversity of global modes of tube contraction that could occur within a given network, based on its geometry and topology, and sensitively identifies when global peristaltic patterns emerge and dissipate.

## 1. Introduction

Despite the lack of a central nervous system, and the many divergences from multicellular animals, the plasmodial slime mold *P. polycephalum* is capable of complex decision making, as it explores space, locates nutrients, and links them together via a network of tubes. *P. polycephalum* plasmodia grow indeterminately, encounter and assimilate food sources, and integrate them into a network that uses materials economically while minimizing the energy costs of transport (Akita et al. 2016). The adaptive network making of *P. polycephalum* has been studied extensively, leading to insights into its ability to find paths through mazes (Nakagaki et al. 2000a; Nakagaki and Guy 2008), solve the two-armed bandit problem (Reid et al. 2016), find shortest paths in environments with variable costs of growth (Bonifaci et al. 2012), and to arrange itself optimally for delivering nutrients (Dussutour et al. 2010; Tero et al. 2010). Additionally, the tube diameters within the network, both reflect the organism's current optimization of flows relative to nutrient sources, and encode information about its previous encounters with food stimuli (Kramar and Alim 2021). Although network morphology has attracted ample research attention, the flows within the

network are relatively less well mapped. An active actomyosin cortex, enables tubes to dynamically vary their radii (Kamiya 1981). Rhythmic contractions can create flows that span the entire network, transporting nutrients and organelles across the organism. Understanding the morphology of the network and the protoplasmic flows it creates are linked challenges, since the topology and radii of tubes within the network both sculpts the protoplasmic flows and continuously adapts to them.

As such, the study of the development of behavior and memory in this simple organism is interesting for illuminating the range of behavioral phenotypes that it may be capable of, and for understanding the mechanisms that underlie how, despite lacking a neural system or any central information processing organ, *Physarum* has a distributed capacity to assimilate and respond to information from its environment. In particular, studies have highlighted how tubes respond to external chemical cues from the organism's environment (Kramar and Alim 2021; Fleig et al. 2022), and to internal stimuli, including chemical signals transported by internal flows, and to the hydrodynamic stresses of the flows themselves (Kamiya et al. 1988; Alim et al. 2017).

In many filamentous fungi, protoplasmic flows are created by water

---

uptake throughout the mycelium, which is then pushed through a network of hyphae to expanding hyphal tips, located at the periphery of the mycelium. This mechanism can produce extremely fast flows in the fastest growing fungi, including speeds of 50 µm/s, up to 100s of *µm/s* in the fast growing asomycete, *Neurospora crassa* (Lew 2005). Multidirectional flows are possible, including flows that alternate in time within a single tube (Schmieder et al. 2019), or that can occur simultaneously within a single hypha, when organelles are trafficked by different motor proteins, or by a combination of motor proteins and bulk protoplasmic flow (Roper and Seminara 2019). By contrast, in *Physarum* plasmodial networks, active pumping, due to rhythmic tube contraction and dilation, propels protoplasm, and can drive it toward or away from the network periphery. Efficient transport on the network-scale may be affected by coordinating contraction phases, to create a traveling or *peristaltic* wave, in which contractions smoothly pass from each tube through its neighbors. Yet, under many conditions, contractions do not coordinate globally, creating small or local protoplasmic flows (Nakagaki et al. 2000b; Matsumoto et al. 2008; Alim et al. 2013).

Two classes of *Physarum* behaviors are subjects of study and modeling, and represent different time scales on which the network adapts to new information about its environment: 1. The coordinated pumping-driven flow of protoplasm (Ueda et al. 1986; Yoshimoto and Kamiya 1984; Kamiya et al. 1988; Ueda et al. 1986) allowing stimulus responses on the scale of minutes (Latty and Beekman 2011; Meyer et al. 2017), including locomotion (Rieu et al. 2015; Lewis et al. 2015; Rodiek et al. 2015; Zhang et al. 2017), and nutrient/chemical signal proliferation (Alim et al. 2017), and 2. The adaptation of network morphology, including tube diameters, densities and connectivities on time scales of 10–30 min (Kramar and Alim 2021). Toward quantitative study of both classes of *Physarum*'s behaviors, we develop a method for measuring the ever-changing network morphology, along with a network-informed approach to mapping the distribution of contractions and dilations across this network.

Although automated analyses of sequences of microscope images allows direct measurement of tube diameters and network morphology, and these data can be analyzed to extract summary information such as, for the network morphology, the levels of modularity or redundancy within the network (Tero et al. 2010), and the phase distributions within tubes when they are contracting with the same frequencies (Alim et al. 2013), the problem of mapping behaviors rapidly becomes enmired in issues of data complexity. For example, descriptors of pumping behaviors must describe time-varying radii in tens or even thousands of individual tubes, not even accounting for the additional geometric complexity created when parts of the same tube have different phases of oscillation. By contrast, when tube oscillations are coordinated across the entire network, as occurs when peristaltic waves emerge, a simple mapping of the distributions of phases may suffice (Alim et al. 2013), but a range of behaviors is possible, from apparent uncoordination to global synchronization, and a focus upon phase renders opaque the pumping behaviors that occur before the emergence of the peristaltic wave, or after its dissipation. Reduced-order descriptors, in which tube oscillations are projected upon a small number of modes, can allow the structure of peristalsis, and the transition between behaviors, to be quantified. But a basis of modes needs to be detected. In Fleig et al. (2022), a spectrum of peristaltic flow modes was identified using Principal Component Analysis (PCA) on sequences of pixel intensities. The PCA identified modes could be used to project pumping patterns, and synchronization of modes sensitively reports on peristalsis's first emergence and its subsequent disappearance. PCA is a broadly useful tool for identifying bases from data, but it is agnostic to the physics of the network—the geometry and connectivities of tubes—and how these physics constrain what types of peristaltic flows the network can create. As such it is difficult to interpret how the modes identified by PCA relate to the organism's changing transportation network, or to unpack the bi-directional coupling between modes of protoplasmic flow and the morphology of the network.

Here, we identify a mapping based on network-wide flow modeling that transforms network measurements to resultant flows, effectively identifying the types of coordinated flows the network can support, and the patterns of tube oscillations that are needed to create them (called **Γ**, the behavior of which is sketched in Fig. 1). Encoded in this mapping are modes that directly identify important peristaltic contraction patterns that contribute most to a rapid response to stimuli. As a proof of concept, we study three brightfield time series (Movies S1, S3, and S5 from Kramar and Alim, 2021) of morphologically diverse organisms over a time scale of many peristaltic patterns. We demonstrate that flow modes and contraction patterns can be followed during network evolution, and can be well represented using our identified bases. In particular, the emergence of globally coordinated modes of contraction can be read out from the time traces of the data presented via our bases, and the times and events that lead to emergence can also be visualized using these modes as they were using previous PCA analysis. At the same time, the spectrum of modes identified by our method is directly controlled by the network geometry. Remarkably, we find that the number of significant modes is affected by the size of the network, but only little by the hierarchy of tube radii within the network. The degree of isotropy of our measured networks may issue from the relative uniformity of the environments in which the networks, studied here, were imaged. Isotropic and relatively uniform network morphologies may themselves be adaptive under conditions where growth is not biased toward or away from sparsely distributed food sources or stressors, allowing the network to respond to foods or stresses encountered from any direction.

## 2. Methods

### 2.1. Mathematical background

In the following, we develop the mathematics behind idealizing flows in a *P. polycephalum* organism as flows on a mathematical network. Here, matrices and vectors are bold-faced with matrices capitalized. All other quantities are scalar.

#### 2.1.1. Flow in an expanding and contracting tube

The rate of flow of homogeneous, incompressible fluid driven by pressure drops through a cylindrical tube is with the Hagen Poiseuille Law, so long as the Reynolds number $\frac{\rho u L}{\mu}$ and the Womersley number $L\left(\frac{\omega \rho}{\mu}\right)^{\frac{1}{2}}$ are sufficiently low as previously justified for *P. polycephalum* (see (Watanabe et al. 2011)). In these definitions, $\rho$ and $\mu$ are the density and dynamic viscosity of the fluid respectively, $L$ is the system length scale, $u$ is the scale of the fluid velocity, and $\omega$ is the frequency of fluid oscillations. $\omega$ relates to the frequency of oscillations exhibited by our measured volume changes in the following, but a direct measurement of it was not performed in the present analysis. The Hagen Poiseuille Law states that the amount of flow $Q$ passing through a tube is proportional to the pressure gradient $\Delta p$ across the tube:

$$Q = \frac{\pi a^4}{8\mu L}\Delta p = \kappa \Delta p \tag{1}$$

where $a$ and $L$ are the radius and length of the tube respectively, and $\mu$ is the dynamic viscosity of the fluid being pushed through the tube. $\kappa = \frac{\pi a^4}{8\mu L}$ is known as the Hagen-Poiseuille conductance of the tube. This simple flow equation, however, must be modified for *Physarum* which is driven primarily by peristalsis and not by differences in pressure. Given a cylindrical tube with a prescribed, dynamic volume $V(t)$, Stokes' equations can be solved to develop a flow formula for flow that now takes into account changes in tube volume (Shapiro et al. 1969; Secomb 1978; Si et al. 2011; Alim et al. 2013):

$$Q(z) = -\frac{dV}{dt}(t)\left(\frac{z}{L}\right) + \kappa \Delta p \tag{2}$$
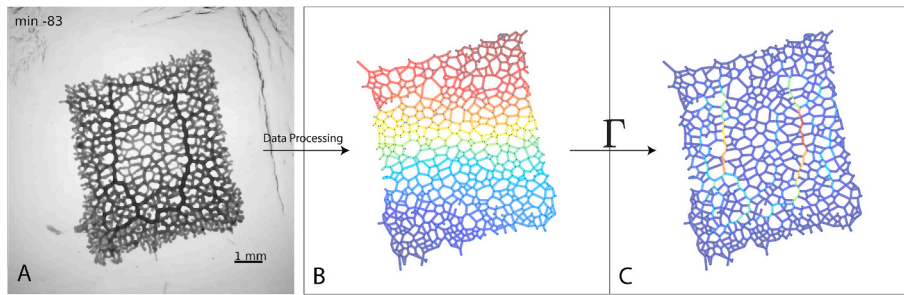
**Fig. 1.** A schematic of the processing pipeline in our method. Shown is taking the first frame of Movie S1, extracting graph morphology, and finding the mode of top importance for our mapping **Γ**. **Γ** takes in a vector of tube contractions or expansions (visualized in B), and outputs a vector of flows (visualized in C). In these visualizations, red corresponds to tube expansion in B and high flow in C; blue corresponds to tube contraction in B, and low flow in C. The mapping itself generates the modes in both B and C once data has been processed.

where $z \in \left[-\frac{L}{2}, \frac{L}{2}\right]$ describes the longitudinal axis, with $z = 0$ measuring the center of the tube.

### 2.1.2. Conservation of mass on a network

We model *Physarum* as a dynamic network $G$ with nodes $V_G$ and edges $E_G$. We define $\langle i, j \rangle \in E_G$ to be the edge connecting node $i$ and node $j$, $\mathbf{K} = (\kappa_{ij})$ to be a matrix containing the Hagen-Poiseuille conductances in edges $\langle i,j \rangle$, $p_i$ to be the pressure at node $i$, and $V_{ij}$ to be the volume of edge $\langle i,j \rangle$. By convention $K_{ij}$ and $V_{ij}$ are zero if $\langle i,j \rangle \notin$ E. We ensure that fluid is neither created nor destroyed by imposing conservation of mass on the entire system, which is ensured by equations enforcing that mass is neither created or destroyed at each node. These equations inform the eventual assignment of pressure at each node, which, paired with designated volume changes, determines flows which precisely conserve mass in the system. In this case, this amounts to asserting that total flow into a node is balanced by total flow out. Using Eq. (2) measured at $z = -\frac{L}{2}$, conservation of mass results in:

$$\sum_{j \in V_G} \kappa_{ij}(p_i - p_j) = -\frac{1}{2}\sum_{j \in V_G} \frac{dV_{ij}}{dt} \qquad (3)$$

This equation is written compactly in vector form as $\mathbf{L_K p} = \mathbf{b}$ where $\mathbf{L_K}$ is the weighted graph Laplacian with weights prescribed by $\mathbf{K}$, $\mathbf{p} = (p_i)$, and $b_i = -\frac{1}{2}\sum_{j \in V_G} \frac{dV_{ij}}{dt}$. This equation can be solved uniquely so long as the graph is connected and a pressure gauge node is prescribed (Forrow et al. 2018). Intuitively, such a gauge node is needed because flows are determined by pressure differences only, and so the problem must be supplied with a node to call "gauge pressure," i.e. the node that defines what all other pressures are compared to.

### 2.1.3. Relating observed volume changes to flows

Section IIA2 gives us the tools to relate observed volume changes to actual flows on the network. We define $Q_{ij}$ to be the flow in edge $\langle i,j \rangle$ measured at the center of the tube, and define the flow to be positive if it goes from node $i$ to node $j$ with $j > i$, and negative otherwise. The flow in each tube measured at the center (i.e. $z = 0$) is linearly related to the pressure gradient across each tube, which in turn is linearly related to the volume change, so a linear relationship between flows and tube volume changes can be calculated. With this definition, $\mathbf{q}$ and $\mathbf{v}$ are vectors containing the flows and volumes of all edges. We may thus derive the linear relationship

$$\mathbf{q} = \Gamma \frac{d\mathbf{v}}{dt} \qquad (4)$$

$\Gamma$, the linear map above, is a function both of tube geometry and network topology. Mathematically, $\Gamma$ may be written in terms of previously-defined quantities as

$$\Gamma_{ij} = -\frac{1}{2}K_{ij}(e_i - e_j)^T \mathbf{L_K^{-1}} \mathbf{B} \qquad (5)$$

where $e_i$ is the $i^{th}$ euclidean basis vector and $\mathbf{B}$ is a matrix such that $B_{ik}$ is 1 if node $i$ is an endpoint of edge $k$, and 0 otherwise. At a given instant in

time $\Gamma$ encodes how the network's observed characteristics—tube expansion/contraction, network topology—transform into the flows that transport fluid through the organism. $\Gamma$ is a dense matrix, which in this case means that a volume change in any edge of the network affects the resulting flow in the rest of the network. The intuition behind how $\Gamma$ produces flows from volume changes is shown in Fig. 2.

### 2.1.4. Analyzing important volume change modes with the mapping Γ

Given that images of *P. polycephalum* induce highly complex networks that contain sometimes over 1000 edges, $\Gamma$ is typically a mapping that operates on extremely high-dimensional space. To make reasonable sense of what $\Gamma$ is doing, it is therefore useful to capture the lower-dimensional essence of $\Gamma$. To do this, we employ the Singular Value Decomposition (SVD), which decomposes $\Gamma$ into many orthogonal mappings and ranks these orthogonal mappings in order of importance by assigning each one a *singular value*. These mappings are referred to in this paper as *component mappings*. The SVD decomposes $\Gamma$ as follows:

$$\Gamma = \mathbf{U\Sigma V^T} \qquad (6)$$

where $\Sigma$ is a diagonal matrix comprised of nonnegative singular values $\sigma_j$, which are typically sorted in descending order from the top left to bottom right of the matrix, and $\mathbf{U}$ and $\mathbf{V}$ are orthonormal matrices whose columns contain the left and right singular vectors of $\Gamma$ respectively. The decomposition is such that, given the $i^{th}$ columns $\mathbf{u_i}$ and $\mathbf{v_i}$ of $\mathbf{U}$ and $\mathbf{V}$, $\Gamma \mathbf{v_i} = \sigma_i \mathbf{u_i}$. The SVD is similar to diagonalization in that important modes can be analyzed, but it has the added benefit that all numbers including singular values are real, so important component mappings can be visualized simply.

The SVD can be used to lower the dimension of a representation of a given matrix by truncating the amount of mappings one wishes to consider. For example, the mapping $\Gamma$ could be (rather poorly) approximated using only 10 degrees of freedom by cutting off all but the first 10 columns of $\mathbf{U}$ and $\mathbf{V}$ and taking the upper-left $10 \times 10$ submatrix of $\Sigma$, then re-multiplying the decomposition. This idea is used extensively in Principal Component Analysis (PCA), but PCA is used for
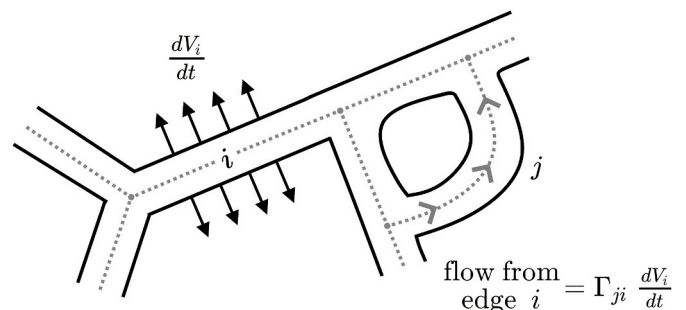


**Fig. 2.** A diagram of how the mapping $\Gamma$ operates on the network. The quantity $\Gamma_{ji} \frac{dV_i}{dt}$ represents the contribution of edge $i$'s expansion or contraction to the flow in edge $j$. Edge $j$'s flow is the sum of contributions from all other edges in the network, i.e. $Q_j = \sum_i \Gamma_{ji} \frac{dV_i}{dt}$.

symmetric matrices whose inputs and outputs are assumed to be from the same space. In contrast, our inputs are networks contractions and outputs flows, so PCA can't be directly used.

Importantly, the SVD also identifies important modes that the mapping acts on. In our case, we use the SVD of the mapping $\Gamma$ to consider the effects of geometry and topology on flow generation given primary volume change modes.

## 2.2. Extracting network information from data

Here we outline the steps taken by our custom Matlab code to extract dynamic morphological information from data.

### 2.2.1. Creating the master network for the video

Over the course of a time sequence of microscope images, some tubes disappear due to pruning, and some disappear and reappear as they lose contrast with the background via contraction. For these reasons, the network's topology changes with time. To account for this, we first need to create a master network that contains all possible tubes that exist over the course of the time sequence. We then define the time-varying networks as subgraphs of this master network. Here it is important to note that our process assumes that the organism doesn't move or change shape with time, which restricts the data we can process to networks that are not migrating.

To create this master network, we take the median of approximately 50 frames exhibiting dense versions of the network to capture an artificial image where contrast between tube and background is ideal for thresholding and noise is dampened. We then create an image mask via adaptive local thresholding (Matlab adaptthres). This mask is then skeletonized to create an image mask whose tubes are only a single pixel thick. Through a custom algorithm similar to the often-used anaskel (Fetterman 2022) called skel2graph (included in the code accompanying this paper), the network topology (i.e. the nodes and the edges of the network) is then extracted from the skeleton. Alongside this network topology, our algorithm also returns a labeled binary image that records the actual geometric shape of each edge for use later in measuring data features.

### 2.2.2. Measuring geometric and topological features for each microscope frame

Armed with the master network, we now proceed to measuring frame-by-frame information. We analyzed three sequences of *Physarum* images (Movies S1, S3, and S5 from (Kramar and Alim 2021)), which were chosen as data because they each demonstrate qualitatively different morphologies and behaviors over the course of the data. Movie S1 is a topologically consistent, densely connected network for the whole video. Movie S3 is topologically consistent as well, but with much less density than Movie S1. Movie S5 demonstrates a marked change in topology after a food stimulus is introduced, and is also fairly densely connected until pruning thins the organism. In the following, we identify morphological and dynamic measurements of these three videos and compare them. For each frame, we again create an image mask with adaptive thresholding. Adaptive thresholding considers a window of pixels around the pixel of interest and forms a threshold to separate foreground and background from grayscale data. We then directly associate each pixel in the mask with an edge from the master network. If an edge has no mask pixels associated with it, it is removed from the network for the given frame.

For each associated edge, we then compute tube volume. In previous works (Alim et al. 2013; Bäuerle et al. 2017; Fleig et al. 2022), tube volume was argued to be inversely correlated to pixel intensity by the Beer Lambert Law, and as such intensity values of each pixels were used as an indirect measurement of tube contraction state. In our application, we utilized a compressed. mp4 video format taken directly from the supplementary materials of (Kramar and Alim 2021), yielding frames that were lower in dynamic range and resolution than previous work.

Intensity measurements on the graph skeleton, therefore, suffered from a low signal-to-noise ratio, and didn't prove very useful as a proxy for volume. To smooth out this noise, we integrated intensities over entire tubes using the following model:

$$Volume = \sum_{i \in tube} DA \frac{I_{0,i}}{I_i} \tag{7}$$

This model reflects the fact that thicker edges are darker, and that the apparent darkness of a pixel reflects how much light is absorbed or scattered in the imaging. The sum is taken over all pixels $i$ that make up the section of the mask associated to a given edge. Here, $D$ is a length scale relating intensity to length, $A$ is the area of each pixel, $I_{0,i}$ is the intensity of the background around pixel $i$ (assumed brighter than a pixel on the tube), and $I_i$ is the intensity of pixel $i$. Mathematically, this is an approximate integral of a height function over an area, which produces a volume. Since we were primarily concerned with measuring volume dynamics and not accurate measures of volume, the scaling constant $D$ was assumed to be 1 for this analysis. With this model in hand, we were able to recapitulate the measurement smoothness shown in previous works even with our compressed data.

We then calculated an average radius for each tube by assuming that tubes are perfectly cylindrical. In this case,

$$radius = \sqrt{\frac{Volume}{\pi L}}$$

where $L$ is the arc length of each skeletonized edge.

Finally, given that our model in Eq (5) relies on volume change dynamics, we computed $\frac{dv}{dt}$. Given that we are interested primarily in expansion/contraction dynamics and not growth, we first detrended our volume data by subtracting off a moving mean of width corresponding to two typical contraction periods. We then smoothed the data via Matlab smoothdata and took a simple finite difference to calculate $\frac{dv}{dt}$ in each edge.

### 2.2.3. Identifying flow modes on $\Gamma$

Armed with frame-by-frame network features, we could then define our matrix $\Gamma$ from Eq. (5) for each frame. To identify the important component mappings of $\Gamma$, we employed the SVD as described in section IIA4. However, given that the total volume of the network is assumed to be conserved, we first restricted our input vectors $\frac{dv}{dt}$ to sum to zero via a projection $\mathbf{P}$ onto the space of volume-conserving vectors. Identifying these volume-conserving modes was then achieved by taking the SVD of $\Gamma\mathbf{P}$. A visual representation of the modes detected in a network consisting of tubes attached end to end is given in Fig. 3. This visualization shows some of the typical features of our modal analysis: the visual similarity of normal modes to some of the eigenmodes of the graph-Laplacian (i.e. discrete sine waves), and the tendency of higher modes to have finer length scale variations in the amount of contraction or dilation. Additionally, single cellular tubes are biologically interesting in their own right; they can be readily realized experimentally, and are a common configuration for a network that is on the verge of migrating.

## 2.3. Relating flow modes frame by frame for dynamic information

Given that the topology of the network is not assumed to be constant from frame to frame, and that the ordering of important modes is also likely to change over time, we devised a way to register similar modes to each other between frames. First, to account for differing network topologies, we only compared modes using edges common between frames via a euclidean distance. Using these calculated mode similarities between two frames, we then solved the linear assignment problem (Duff and Koster 2001) to register modes to one another frame-by-frame. Due to the complexity of the problem, we restricted this dynamic analysis to the top 20 modes of the mapping. This assignment allowed us
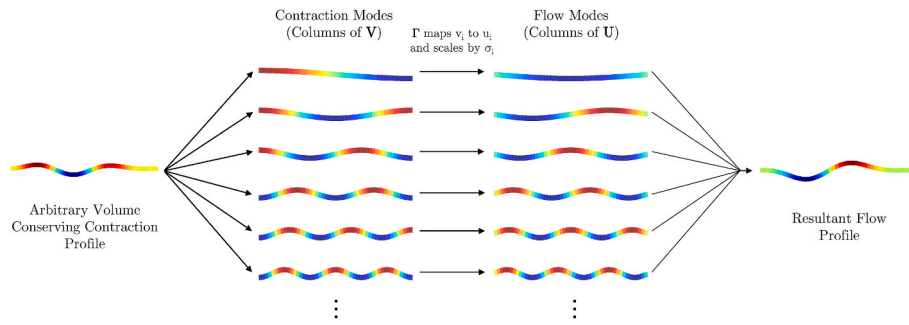
**Fig. 3.** A singular value decomposition of a network of 50 tubes connected end to end. We visualize the modes of the SVD of Γ computed on a random volume-conserving selection of tube contractions to demonstrate the features that the SVD is capturing when it computes modes.

to form the continuous mode coefficient plots visualized in Fig. 7.

## 3. Results

First, we derived a physical model that incorporated changing tube contraction states into flow calculations. This model resulted in a linear map, **Γ** (Eq. (5)), that takes instantaneous contraction rates as input and outputs networkwide cytoplasmic flow. The modes and singular values analyzed in the following are those of this mapping **Γ**, and represent a whole-body analysis of the connection between network morphology——encoded in **Γ**—and dynamics. Further details on **Γ** are included in section II.

We analyzed three sequences of *Physarum* images (Section II.B.2), which were chosen as data because they each demonstrate qualitatively different morphologies and behaviors over the course of the data. Movie S1 is a topologically consistent, densely connected network for the

whole video. Movie S3 is topologically consistent as well, but with much less density than Movie S1. Movie S5 demonstrates a marked change in topology after a food stimulus is introduced, and is also fairly densely connected until pruning thins the organism. In the following, we identify morphological and dynamic measurements of these three videos and compare them.

### 3.1. Topological and geometric measurements

To identify the dynamical function of network morphology, we utilized the singular value decomposition (SVD) of the modeled mapping (**Γ** from Eq. (5)) that takes as input network contraction dynamics and outputs cytoplasmic flows through the network. The **Γ** matrix encodes both network geometry and topology via inclusion of the weighted graph Laplacian, and so an analysis of **Γ** is an analysis of the function of the particular network morphology, in determining how many flow
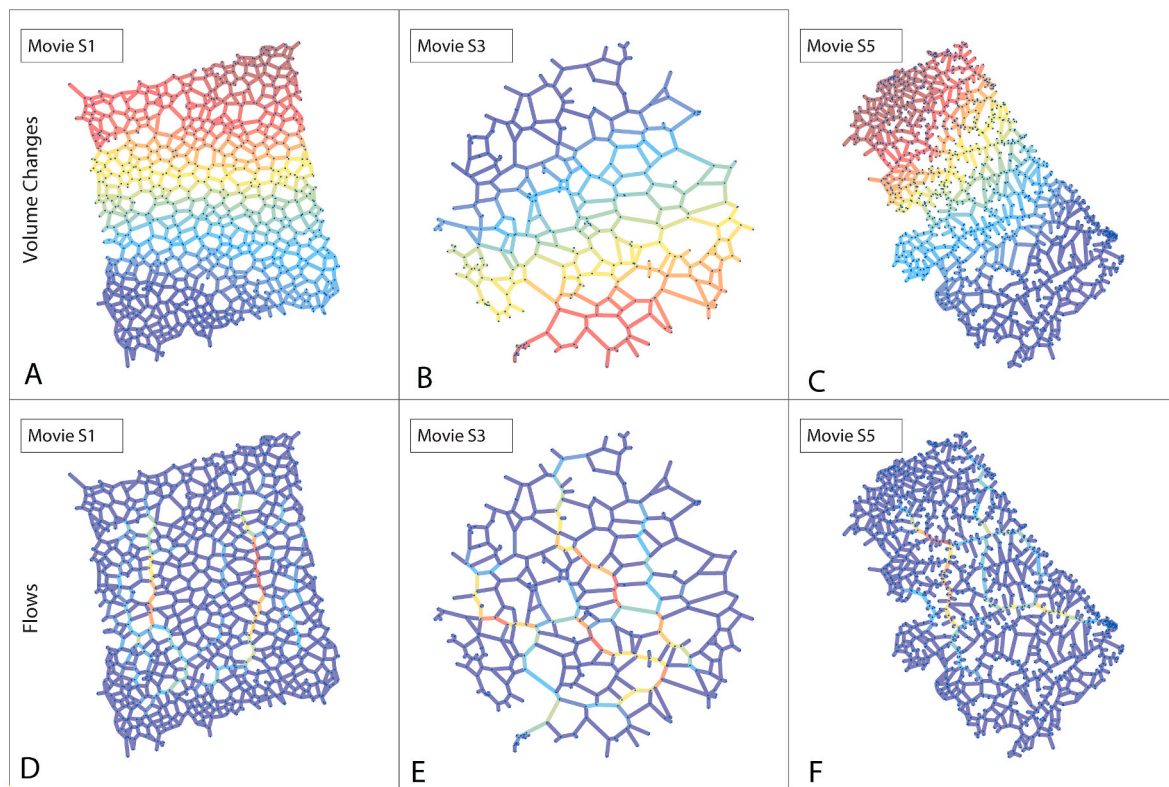


**Fig. 4.** Visualized are the top component mappings of **Γ** for frame 1 of all 3 of our datasets. Red indicates tube expansion or high flow, blue represents tube contraction or low flow. (A–C) the right singular vectors of **Γ**, corresponding to contraction/expansion patterns that lend themselves to produce the highest flow. (D–F) the absolute values of the left singular vectors of **Γ**, corresponding to the distribution of flows created by the particular contraction/expansion patterns above them. Tubes that get the most flow (colors that are not deep blue) correspond to thicker tubes in the dataset.

modes a single network can support by tube contractions and dilations. The SVD of $\Gamma$ ranks important contraction distributions by the relative sizes of the flows they are able to produce in the network.

What do these contraction distributions look like? Our model shows that linear variations in contraction velocities produce largest flows. In Fig. 4, we observe that, despite different shapes and topologies, the highest ranked mode of $\Gamma$ takes a linear gradient of contractions (top row) and creates flow along the thickest tubes that are approximately parallel to gradient direction (bottom row). Although the patterns of contraction (modes) seem to be little influenced by the hierarchies of tube radii present within the network, the flows associated with modes of contraction (Fig. 4D–F) are channeled substantially through the thickest vessels of the organism, affirming the importance of these high radius vessels to network-wide transport *P. polycephalum*.

The spectrum of singular values of $\Gamma$ measures the number of different modes of contraction and dilation the network can support, and is a functionally important readout of the network's shape. Specifically, we focus on how many modes are needed to describe the entire $\Gamma$ mapping. Following conventions adopted in other mode-analyses, such as PCA, we determine the number of modes needed to make up 90% of the total map magnitude. Mathematically, finding this number is equivalent to taking the cumulative sum of the singular values in descending order and stopping when you reach 90% of the total singular value sum. For all three of the mapped networks, and over all time points, the percentage of singular values needed to take up 90% of the total singular value sum was between 43% and 47% of the total number, which is simply the number of edges within the network.

To further understand *Physarum*'s spectrum of singular modes, and how it varies over time and between different *Physarum* individuals, we plot the singular values themselves, in descending order for a variety of conditions. We first plot the spectrum as a function of the absolute mode index, a number that ranges from 1 to the number of edges in the network (Fig. 5). The blue areas enclose the upper and lower quantile of the singular values for the entire time series, sampled every ten frames. Consistent with our analysis of the number of significant singular values, we found the spectrum to be extremely broad, with the singular value of mode $n$ best fit by a power law: $n^{-2/3}$.

To probe the influence of the network structure, we first compare the spectra of real *Physarum* with synthetic networks in which we permute tube radii across the entire network, leaving the total variance in tube radii unaffected, but randomly disconnecting high conductance pathways and thus any spanning trees that the network may contain (Fig. 5, red regions: upper and lower quantiles of the ordered singular values). The blue and red regions show considerable overlap, indicating that the singular values are mostly unaffected by a shuffling of radii throughout the network. This overlap suggests that the specific arrangement of high conductance tubes within the network does not influence the structure

of its most effective patterns of contraction, and nor does it strongly affect the scale of flows that these most effective modes can create within the network. Instead, the data suggest that the network is mostly isotropic. Given that most protoplasmic flow is predicted to be contained in the thickest tubes, as indicated in Fig. 4, isotropy of the thickest tubes may allow the network to push fluid in any or all directions when it encounters a new food source.

Although the precise arrangement of high conductance tubes is little distinguishable from isotropic arrangements, the presence of tube radius hierarchies strongly affects the magnitudes of flows created within the network. To probe the contribution of tube radii, we compare real networks with a second class of synthetic network, in which all tubes are uniformly given the same radius (black shaded curves in Fig. 5). Uniform networks are markedly lower than the correspondent hierarchical networks for the first few hundred modes, about 400 for Movie S5 and 250 for Movie S3. Singular values of $\Gamma$ correspond directly to the amount of flow that a given unit network contraction can create, and so lower singular values in the black region indicate that networks with uniform thickness can produce less flow for a given contraction pattern than those with radius hierarchy. The continuous spectrum of modes, too, creates flows in a variety of different directions. Combined with the importance of radius hierarchy, we observe that *Physarum*'s morphology is optimized to produce high flows in any direction.

We also study how the spectrum of singular values varies with time. Movie S5 shows a large organism that prunes itself drastically over the course of the dataset after food is introduced. During this drastic change in topology, we observe self-similar changes in the spectrum of singular values. Shown in the top left of Fig. 6 in blue is the cumulative sum of the singular values in descending order for every 10 frames of the video. As edges are pruned the total number of modes goes down (total number of modes is equal to total number of edges), as does the total sum of singular values. However, if the cumulative sum of singular values is normalized by the total sum, and the modes as a fraction of the total modes (Fig. 6 B), the curves collapse into a single blue band. An alternative framing of this result is that in the starting and in the pruned networks, the relative contributions of any percentage of modes to the total cumulative value sum remain constant. This is not an obvious result and further analysis of $\Gamma$ may elucidate why its spectrum is invariant in this way, to pruning. Pruning has hitherto been assumed to be a coarsening process, that grows the largest tubes at the cost of the smallest. Described in this way, we would expect it to emphasize stronger modes and suppress weaker modes, changing the shape of the spectrum.

We see the same self-similarity in the changing singular value spectrum over time for the entirety of Movie S3 (Fig. 6 C, D). The plasmodial network in Movie S3 does not experience significant tube pruning, but it does demonstrate a significant increase in visible cross-
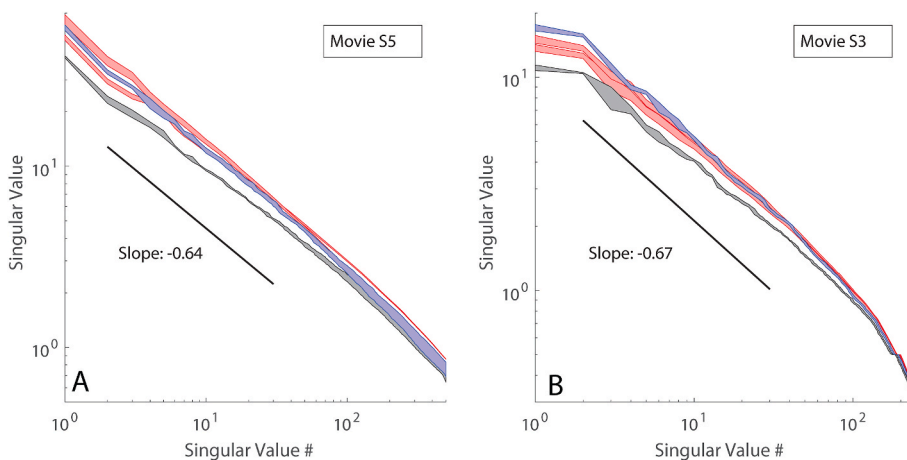


**Fig. 5.** Singular values are plotted in descending order for a variety of conditions. The blue shape is the interquartile range of singular values for every 10 frames in both datasets. The black shape is the interquartile range of singular values (measured every 10 frames) when all radii in the network are set equal to their mean. The red shapes are the interquartile ranges of the singular values of synthetic networks whose radii have been randomly permuted 100 times both before and after food is added, hence the reason two seemingly distinct red shapes appear. Panel A: red regions are taken from synthetic networks coming from permutations of radii in frames 761–821 and 2471–2531 of Movie S5, sampled every ten frames. Panel B: red regions are taken from synthetic networks coming from permutations of radii in frames 461–491, 511–531, and 2871–2931 of Movie S3, sampled every ten frames.
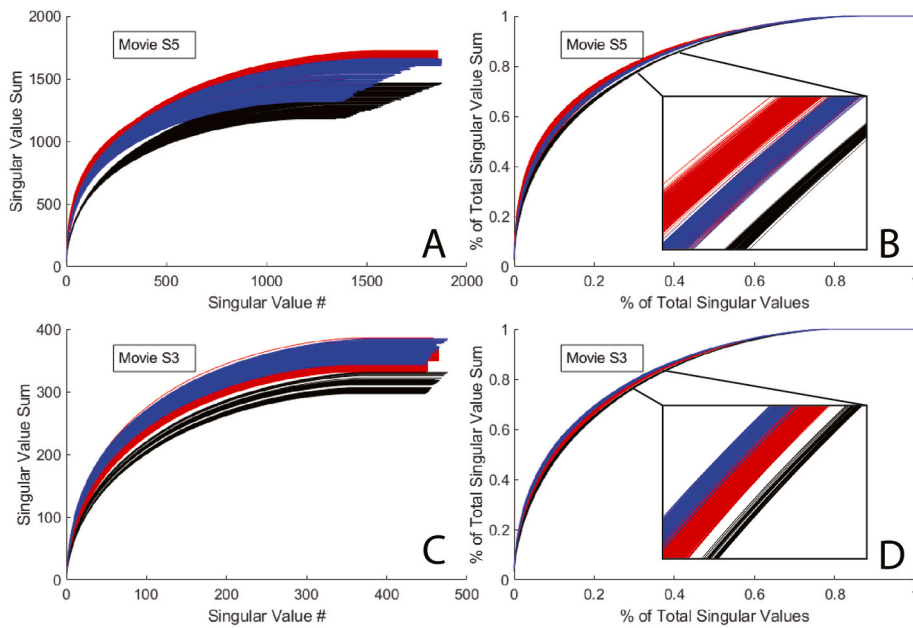
**Fig. 6.** Singular value distributions, both scaled and unscaled, are plotted for Movies S3 and S5. In all plots, red lines are synthetic graphs with radii of edges randomly permuted, black lines are synthetic graphs whose radii are all set to the average radii for the given frame, and blue lines are actual singular value distributions for measured radii. For blue and black lines, data is measured every ten frames for the entirety of the dataset. For red lines, 100 random permutations are generated for a selection of frames before and after food is added. (A and B) red lines are taken from permutations of radii in frames 761–821 and 2471–2531 of Movie S5, sampled every ten frames. (C and D) red lines are taken from permutations of radii in frames 461–491, 511–531, and 2871–2931 of Movie S3, sampled every ten frames. (A and C) cumulative singular value sum of singular values in descending order is plotted versus singular value number. (B and D) same as the A and C, except the *x* and *y* axis have been scaled down by number of singular values and total singular value sum, respectively.

organism peristalsis. That the mode spectrum in both organisms changes self-similarly, may reflect constraints in how strongly the singular values of $\mathbf{\Gamma}$ can be localized in a small number of modes, further supporting the inferences made before, that the specific arrangements of tubes and their radii have little effect on the singular modes. We cannot rule out, however, that tube hierarchy has undetected importance, and that the invariance of the spectrum of singular values under pruning and other network changes, reflects some symmetry of how pruning and other network changes operate on different scales of tubes.

The synthetic networks created for Fig. 6 A, C (red), by permuting the tube conductances in real networks, collapse to the same master curve as real networks after normalization rescaling in both the network shown in Movie S5 (Fig. 6 B), and the network shown in Movie S3 (Fig. 6 D). The spectra at different time points overlap for real and synthetic networks over most of the significant singular values, and though the real network has a slightly broader spectrum than the synthetic network in S5, the places are reversed in S3, suggesting that there is no significant difference between the normalized spectra. Conversely, in synthetic networks with uniform radii (black lines in Fig. 6), the spectrum lies slightly underneath both real and permuted spectra, both with and without normalization. This small difference, consistent between the two networks suggests that the singular values of the top modes of the uniform network are not as top-heavy, suggesting that mild selection occurs for the first few modes in networks with some radius hierarchy.

### 3.2. Measuring emergence of coherent pumping

Spectral analysis of $\mathbf{\Gamma}$ gives us a readout of what internal flows a network can generate through tube radius changes. When real measured volume changes are projected onto these modes, they provide a reduced basis for describing the pumping that occurs in the network. A complication here is that, as shown in section IIB, the topology of the measured network changes frame-by-frame, albeit by the gain or loss of only a handful of edges among hundreds for the networks analyzed here. Because of network changes, $\mathbf{\Gamma}$'s matrix representation changes size over time. However, although the total number of contraction modes changes over time, we find that the most important calculated contraction modes maintain their order, and approximately, their singular values. We proceeded, therefore, to analyze the coefficients of the projections of the data onto the top 20 modes of the system (see section IIC) during intervals in which we visually identified the emergence of coherent tube

oscillations. Movies S1 and S3 were chosen because they contain sections of video centered around both the introduction of food and also visual peristaltic waves moving through the organism. The coefficients of the first modes are shown for excerpts of both video sequences in Fig. 7.

How does the presence or absence of visual peristalsis affect the readout of our mode coefficients? Movie S3 probes a rather stable, circular network with barely perceptible contraction dynamics before food is added. At frame 500 (minute 0), food is added outside of the frame, and coordinated peristaltic contraction patterns become visible. Movie S3's mode coefficients (Fig. 7 A) at the moment of food introduction show clean oscillatory behavior in line with the previously measured peristaltic frequency of about 90 s (30 frames) (Alim et al. 2013). We see the mode coefficients reflecting the visual emergence of coordinated peristalsis: around 240s (80 frames) following the introduction of the cue the amplitude of all coefficients increases X-fold. Amplitude increases are greatest for the top modes, showing that pumping occurs preferentially in the modes with greatest flow creation potential (i.e. greatest singular values).

Movie S1's mode coefficients (Fig. 7 B) show the emergence of coherent pumping from initially highly disordered contractions. Visually in the large, dense network imaged in Movie S1, contraction patterns appear random across the organism. There are brief instances, however, when a cross-organism peristaltic wave presents itself—here we see one such instant at around minute −4 (around frame 1900) of the video. Before this instant, we see large-amplitude, unaligned oscillations on the order of 10–15 frames which could likely come from a mixture of uncoordinated pumping and aliased (noisy) data. When organism-wide pumping is observed, we observe clear, coherent oscillations whose period (90 s) matches published data on *Physarum* time-oscillations. It is as of yet unclear what stimulus, if any, triggered the appearance of coherent contractions, as food had not yet been added, nor what triggered their disappearance.

Results from our modal analysis are qualitatively consistent with previous descriptions of *Physarum* behavior. Specifically, we find that in networks presented with no food source, tube wall oscillations may be coherent, with small amplitudes (S3), or incoherent, likely presenting as high frequency modes due to a combination of noise and aliasing effects (S1). When presented a food source, we see existing coherent multimodal oscillations gain amplitude. Coherent multimodal oscillations emerge from noise and disappear spontaneously. We obtain additional
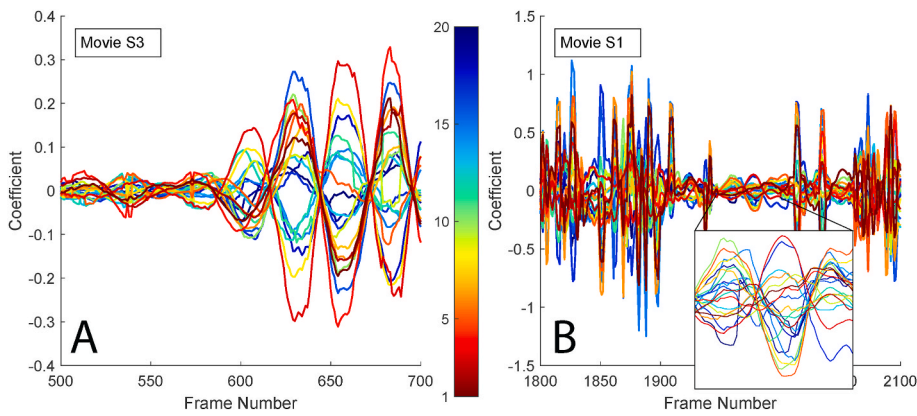
**Fig. 7.** The top 20 mode coefficients are visualized for Movies S1 and S3. Colorbar shows ordering of modes from first (red) to 20th (blue). (A) Movie S3's coefficients form coherent oscillations throughout, increasing in amplitude over the excerpted frames. Lower modes attain higher amplitudes. (B) mode coefficients in Movie S1 are only intermittently coherent. The data corresponding to periods in the video without clear and visible peristaltic contraction patterns do not seem to show oscillation. The long period of coherent oscillation corresponds to a visible peristaltic wave in the video.

quantitative data on the time delays between the food source being presented, and the amplification of coherent oscillations, as well as on the suddenness of amplitude increase.

## 4. Discussion

Coordinated contractions of tubes in *P. polycephalum* enable the organism to achieve a remarkable repertoire of behaviors, including generating network-wide transport of nutrients and protoplasm, whole organism migration and network remodeling. Here, we develop a new tool for quantifying how many network-wide contraction patterns a single organism is capable of, anatomizing those patterns, and identifying, instant-by-instant, which modes are active within the network. Our method originates in a linear mapping, $\Gamma$ that ties together all of *P. polycephalum*'s directly measurable quantities—topology, geometry, contraction dynamics— into an easily-interpretable and mechanistic model of fluid flow. The mapping generates theoretical contraction modes for the given network morphology that are ranked by how much flow they create and thus may be linked to notions of efficiency of transport that have already been extensively studied for the organism (Grebecki and Cie'slawska 1978; Watanabe et al. 2011; Bonifaci et al. 2012; Alim et al. 2013; Baumgarten and Hauser 2013). Our identified flow modes correspond remarkably well to purely data-driven measurements of contraction modes. Since $\Gamma$ also directly computes the flows that arise from these contraction distributions, when paired with data, $\Gamma$ can be used as a measure of how much the network is working to transport fluid at any time.

The modes of $\Gamma$ can be interpreted as the directions in which contractions can most readily generate flows within the network. The modes are readily computed via singular value decomposition, and the spectrum of modes reflects the range of flows that a network is able to easily support. We find that the greatest flow (largest singular value) modes align with the optimal peristaltic phase distribution of (Alim et al. 2013), being a linear gradient of contraction strengths.

Although our findings are confluent with previous qualitative and quantitative descriptions of *Physarum* behaviors, they go beyond existing analyses and methods, such as PCA. Importantly we may interpret the modes of $\Gamma$ as directions in which the large internal flows may be created, allowing the contraction pattern of the network to be physically linked to its architecture. Analysis of pumping modes through the mapping $\Gamma$, highlights the role that network hierarchy plays in creating directions of greatest flow.

Surprisingly, we found the spectrum of possible modes within all of the analyzed networks to be remarkably broad; and that the number of significant singular values was not strongly affected by the hierarchy of tube radii seen within the network. This result should not be interpreted to mean that tube radii hierarchies are unimportant, since the singular values of the (real) hierarchical networks are greater than in (synthetic) networks in which all tube radii are made uniform. So hierarchies of

tube radii allow larger flows to be created within the network, meaning that they increase the flow response to changes in tube radii. Yet, we found relatively small differences between the spectra of real hierarchical networks, and those of variable-tube networks in which all tube radii had been randomly permuted. Our results highlight the need for future mathematical analysis of what features of a graph determine its $\Gamma$-spectrum: including of the relationship between the $\Gamma$-spectrum and the spectrum of the network's graph Laplacian, and study of the roles played by network topology, such as the adjacencies of tubes or their density, and by the shape of the network's boundary.

The insensitivity of the $\Gamma$-spectrum to vessel hierarchy is somewhat at odds with previous work that has stressed importance of the largest vessels in setting the flows that occur within a network, and which have motivated previous studies that reduce the network to a tree for analysis (Tero et al. 2010; Woodhouse et al. 2016; Forrow et al. 2017). Conversely, our calculated modes of tube contractions and dilations are not affected by the degree of radius difference between the largest and smallest tubes in the network, and consist of simple gradients of tube volume changes across the organism. The lack of appearance of the largest diameter tubes in the principal modes, suggests rather that approximating the network as having uniform tube radius, or even as a material continuum, may be pursued as a way to obtain relatively accurate approximations of the most efficient contraction modes, and indeed that these modes may be calculable only from the shape of the organism's boundary. This conclusion may seem at odds with previous theoretical and experimental work (Tero et al. 2010; Woodhouse et al. 2016; Forrow et al. 2017) that has emphasized the importance of tube hierarchies, we note that over longer time scales than are analyzed here, hierarchies of tube radii shape the network's morphological adaptation since hierarchies affect the hydraulic stresses in vessels, which determine which vessels are pruned (Marbach et al. 2023). Hierarchies of tube radii are certainly important to calculating the flows created by the principal modes of contraction, with the largest tubes funneling flows created by the modes of contraction and dilation (Kramar and Alim 2021).

The spectrum is also surprisingly broad, again reflecting the fairly minor role played by the hierarchy of tube radii in selecting particularly favorable modes of tube contraction and dilation. This result, though largely consistent with the broad spectra that were previously identified through PCA analysis (Fleig et al. 2022), sounds two notes of caution: first, even if we accept that flows within the network are confined to a fairly narrow band of possible modes (Forrow et al. 2017), it does not automatically follow that the patterns of contraction used by the network to create these flows are similarly constrained in diversity. Second, the potential utility of modal analysis to reduce high dimensional data on the velocities of contraction of every individual tube, to low dimensional subspaces capable of completely describing every pattern of contraction that we might observe within the real network, is unlikely to be realized. In its place, our analysis emphasizes the breadth

of the space needed to describe *Physarum*'s behavioral repertoire, and its potential responses to new cues from its environment, and echo (Fleig et al. 2022), in suggesting that this space allows for an extremely large array of behavioral responses, with no clear distinction between the important and the unimportant.

These spectral features may reflect the life history stages in which experimental data was collected, in the main video sequences analyzed here, a cut *Physarum* network is imaged before and shortly after it encounters a new food source. Accordingly, the networks that are mapped here may be adapted toward isotropic vessel arrangements, since both the direction in which new food will arrive, and the directions with which nutrients will need to be transported, are not known to the network. In addition to the natural mathematical progressions suggested above, biologically it would be interesting to contrast the results presented here, largely confined to initially static networks that then assimilate small numbers of food sources, with analysis of how the number of modes in the spectrum evolves when a network undergoes substantial pruning – i.e. that encounters and assimilates disparate and wide spread food sources, and where the dominant form of morphological adaptation is one of vessel loss to build an optimal linking network (Tero et al. 2010). In these networks, adaptation may be for a small number of peristaltic modes, as the network organizes itself around a known, small, set of known food sources, rather than in preparation to encounter new food sources.

Since the matrix $\Gamma$ is new to this study, ongoing work is necessary to find how the real *Physarum* networks compare with other model networks. However, $\Gamma$ is partly based upon the inverse Laplacian, the spectrum of which has been characterized for many model networks. Our spectrum, whose modes decay like $n^{-2/3}$, is much broader than for empirical scale free networks for which (McGraw and Menzinger 2008) measures that the eigenvalues of the inverse Laplacian scale approximately like $n^{-3}$. They are even broader than the spectrum of Laplacian eigenvalues for a totally homogeneous network. In the limit of large networks, we would expect this spectrum to approach to the spectrum of the inverse Laplace operator on 2D domain. Absent strong asymmetries of shape, the Laplace operator has eigenvalues $\lambda_{m,n} = \frac{4\pi^2}{L^2}(l^2 + m^2)$, where $l$, $m$ are the wave numbers in two orthogonal directions. Hence, the inverse Laplacian for a uniform network has $O(N^2)$ eigenvalues that are larger than $1/N$ and, correspondingly, we would expect that the $n$th eigenvalue of the operator would be $\sim n^{-1/2}$, which decays only a little slower than our measured spectrum. Further analysis is needed to disentangle how much of the difference is due to the structure of our operator, and how much of the difference is due to structural features of *Physarum* networks.

We add some notes of caution about the kinds of behavioral data for which our method can provide quantification. The results in this paper are derived from compressed video files, at typical resolutions of 70–200 pixels per millimeter, and since tube diameters are on the order of 0.05 mm (as few as 4 pixels) to 0.2 mm, pixel noise in the radii of individual tubes is visible in some of the data. When spectral expansions are performed on the contraction dynamics, aliasing effects occur, in which we fail to see the expected decay of mode amplitudes across modes and in fact, there is apparently high frequency ringing in modes. Thus, although the emergence of concerted patterns of peristalsis leads to clear signals, we can not dismiss that the high frequency oscillations in Fig. 7 result from processing noisy measurements, rather than reflecting real patterns of organization of contractions. Careful assessment of the quality of data is important before using this, or any spectral method, since in every mode, the coupling of contractions across all tubes means that small measurement errors in the finest scales can produce contaminating signals in any mode. In further analysis we will seek to apply our model to high resolution microscope images, and to develop anti-aliasing that filters out the smallest scale contractions when projecting contraction data onto our modes.

We leave for future work the use of $\Gamma$-modal analysis on a wider variety of data, especially sequences in which the network is allowed to travel in search of new food sources. Even when networks are not migrating, quantification of memory and long term behaviors requires tracking contraction modes over longer time sequences, during which the topology of the network can change. In this study, we were able to project tube radius changes onto a small set of modes that remained relatively constant over the entire sequence of the video. Mode ordering is not in general guaranteed, when the $\Gamma$ matrix varies, due to the altering plasmodial network. Alternative data assimilation methods, including Multi-Hypothesis Tracking (Coraluppi 2015), may allow the challenges associated with time-varying modes, to be overcome.

## Declaration of competing interest

The authors declare the following financial interests/personal relationships which may be considered as potential competing interests: Ryan Wilkinson reports financial support was provided by Human Frontier Science Program. Matthew Koziol reports financial support was provided by Human Frontier Science Program. Karen Alim reports financial support was provided by Human Frontier Science Program. Marcus Roper reports financial support was provided by Human Frontier Science Program.

## Acknowledgements

## References

Akita, D., Kunita, I., Fricker, M.D., Kuroda, S., Sato, K., Nakagaki, T., 2016. Experimental models for Murray's law. J. Phys. Appl. Phys. 50, 024001.

Alim, K., Amselem, G., Peaudecerf, F., Brenner, M.P., Pringle, A., 2013. Random network peristalsis in Physarum polycephalum organizes fluid flows across an individual. Proc. Natl. Acad. Sci. USA 110, 13306.

Alim, K., Andrew, N., Pringle, A., Brenner, M.P., 2017. Mechanism of signal propagation in Physarum polycephalum. Proc. Natl. Acad. Sci. USA 114, 5136.

Bäuerle, F.K., Kramar, M., Alim, K., 2017. Spatial mapping reveals multi-step pattern of wound healing in Physarum polycephalum. J. Phys. Appl. Phys. 50, 434005.

Baumgarten, W., Hauser, M.J., 2013. Functional organization of the vascular network of Physarum polycephalum. Phys. Biol. 10, 026003.

Bonifaci, V., Mehlhorn, K., Varma, G., 2012. Physarum can compute shortest paths. J. Theor. Biol. 309, 121.

Coraluppi, S., 2015. Fundamentals and advances in multiple-hypothesis tracking. In: NATO STO IST-134 Lecture Series on Advanced Algorithms for Effectively Fusing Hard and Soft Information. NATO Collaboration and Support Office.

Duff, I.S., Koster, J., 2001. On algorithms for permuting large entries to the diagonal of a sparse matrix. SIAM J. Matrix Anal. Appl. 22, 973.

Dussutour, A., Latty, T., Beekman, M., Simpson, S.J., 2010. Amoeboid organism solves complex nutritional challenges. Proc. Natl. Acad. Sci. USA 107, 4607.

Fetterman, M., 2022. Anaskel Written in Matlab.

Fleig, P., Kramar, M., Wilczek, M., Alim, K., 2022. Emergence of behaviour in a self-organized living matter network. Elife 11, e62863.

Forrow, A., Woodhouse, F.G., Dunkel, J., 2017. Mode selection in compressible active flow networks. Phys. Rev. Lett. 119, 028102.

Forrow, A., Woodhouse, F.G., Dunkel, J., 2018. Functional control of network dynamics using designed Laplacian spectra. Phys. Rev. X 8, 041043.

Grebecki, A., Cieślawska, M., 1978. Plasmodium of Physarum polycephalum as a synchronous contractile system. Cytobiologie 17, 335.

Kamiya, M., 1981. Physical and chemical basis of cytoplasmic streaming. Annu. Rev. Plant Physiol. 32, 205.

Kamiya, N., Allen, R., Yoshimoto, Y., 1988. Dynamic organization of Physarum plasmodium. Cell Motil Cytoskeleton 10, 107.

Kramar, M., Alim, K., 2021. Encoding memory in tube diameter hierarchy of living flow network. Proc. Natl. Acad. Sci. USA 118, e2007815118.

Latty, T., Beekman, M., 2011. Speed–accuracy trade-offs during foraging decisions in the acellular slime mould Physarum polycephalum. Proc. Biol. Sci. 278, 539.

Lew, R.R., 2005. Mass flow and pressure-driven hyphal extension in neurospora crassa. Microbiology 151, 2685.

Lewis, O.L., Zhang, S., Guy, R.D., Del Alamo, J.C., 2015. Coordination of contractility, adhesion and flow in migrating Physarum amoebae. J. R. Soc. Interface 12, 20141359.

Marbach, S., Ziethen, N., Bastin, L., Bäuerle, F.K., Alim, K., 2023. Vein fate determined by flow-based but time-delayed integration of network architecture. Elife 12, e78100.

Matsumoto, K., Takagi, S., Nakagaki, T., 2008. Locomotive mechanism of Physarum plasmodia based on spatiotemporal analysis of protoplasmic streaming. Biophys. J. 94, 2492.

McGraw, P.N., Menzinger, M., 2008. Laplacian spectra as a diagnostic tool for network structure and dynamics. Phys. Rev. 77, 031102.

Meyer, B., Ansorge, C., Nakagaki, T., 2017. The role of noise in self-organized decision making by the true slime mold Physarum polycephalum. PLoS One 12, e0172933.

Nakagaki, T., Guy, R.D., 2008. Intelligent behaviors of amoeboid movement based on complex dynamics of soft matter. Soft Matter 4, 57.

Nakagaki, T., Yamada, H., T'oth, Á., 2000a. Maze-solving by an amoeboid organism. Nature 407, 470.

Nakagaki, T., Yamada, H., Ueda, T., 2000b. Interaction between cell shape and contraction pattern in the Physarum plasmodium. Biophys. Chem. 84, 195.

Reid, C.R., MacDonald, H., Mann, R.P., Marshall, J.A., Latty, T., Garnier, S., 2016. Decision-making without a brain: how an amoeboid organism solves the two-armed bandit. J. R. Soc. Interface 13, 20160030.

Rieu, J.-P., Delanoë-Ayari, H., Takagi, S., Tanaka, Y., Nakagaki, T., 2015. Periodic traction in migrating large amoeba of Physarum polycephalum. J. R. Soc. Interface 12, 20150099.

Rodiek, B., Takagi, S., Ueda, T., Hauser, M., et al., 2015. Patterns of cell thickness oscillations during directional migration of Physarum polycephalum. Eur. Biophys. J. 44, 349.

Roper, M., Seminara, A., 2019. Mycofluidics: the fluid mechanics of fungal adaptation. Annu. Rev. Fluid Mech. 51, 511.

Schmieder, S., Stanley, C.E., Rzepiela, A., van Swaay, D., Sabotič, J., Nørrelykke, S.F., deMello, A.J., Aebi, M., Künzler, M., 2019. Bidirectional propagation of signals and nutrients in fungal networks via specialized hyphae. Curr. Biol. 29, 217.

Secomb, T.W., 1978. Flow in a channel with pulsating walls. J. Fluid Mech. 88, 273.

Shapiro, A.H., Jaffrin, M.Y., Weinberg, S.L., 1969. Peristaltic pumping with long wavelengths at low Reynolds number. J. Fluid Mech. 37, 799.

Si, X., Zheng, L., Zhang, X., Li, M., Yang, J., Chao, Y., 2011. Multiple solutions for the laminar flow in a porous pipe with suction at slowly expanding or contracting wall. Appl. Math. Comput. 218, 3515.

Tero, A., Takagi, S., Saigusa, T., Ito, K., Bebber, D.P., Fricker, M.D., Yumiki, K., Kobayashi, R., Nakagaki, T., 2010. Rules for biologically inspired adaptive network design. Science 327, 439.

Ueda, T., Matsumoto, K., Akitaya, T., Kobatake, Y., 1986. Spatial and temporal organization of intracellular adenine nucleotides and cyclic nucleotides in relation to rhythmic motility in Physarum plasmodium. Exp. Cell Res. 162, 486.

Watanabe, S., Tero, A., Takamatsu, A., Nakagaki, T., 2011. Traffic optimization in railroad networks using an algorithm mimicking an amoeba-like organism. Physarum plasmodium, Biosystems 105, 225.

Woodhouse, F.G., Forrow, A., Fawcett, J.B., Dunkel, J., 2016. Stochastic cycle selection in active flow networks. Proc. Natl. Acad. Sci. USA 113, 8200.

Yoshimoto, Y., Kamiya, N., 1984. Atp-and calcium-controlled contraction in a saponin model of Physarum polycephalum. Cell Struct. Funct. 9, 135.

Zhang, S., Guy, R.D., Lasheras, J.C., Del Alamo, J.C., 2017. Self-organized mechano-chemical dynamics in amoeboid locomotion' of Physarum fragments. J. Phys. D Appl. Phys. 50, 204004.